Journal of Alloys and Compounds 825 (2020) 154025

Contents lists available at ScienceDirect

Journal of Alloys and Compounds

journal homepage: http://www.elsevier.com/locate/jalcom

Laser processing as a high-throughput method to investigate microstructure-processing-property relationships in multiprincipal element alloys

Mu Li [a], Katharine M. Flores [a, b, *]

[a] Department of Mechanical Engineering and Materials Science, Washington University in St. Louis, St. Louis, MO, 63130, USA
[b] Institute of Materials Science and Engineering, Washington University in St. Louis, St. Louis, MO, 63130, USA

ARTICLE INFO

Article history:
Received 10 August 2019
Received in revised form
26 December 2019
Accepted 23 January 2020
Available online 25 January 2020

Keywords:
High-entropy alloys
Direct laser deposition
Microstructure
Mechanical property

ABSTRACT

A direct laser deposition processing method was applied to construct compositional and microstructural libraries of $Al_xCoCrFeNi$ in an efficient and high-throughput manner. Among the compositions ($x = 0.51-1.25$) and quench rates (26–6400 K/s) studied, most of the laser deposited alloys exhibit a cellular microstructure, similar to the cast materials. The microstructural feature sizes were found to follow a power law relationship with the quench rate. The dependence of the microhardness on microstructural length scale was also investigated and observed to follow a Hall-Petch relationship. This study indicates that laser processing is an effective method for rapidly and efficiently evaluating multiprincipal element alloys and their microstructures.

© 2020 Elsevier B.V. All rights reserved.

1. Introduction

Multiprincipal element alloys (MPEAs), also known as "high entropy" alloys, are chemically disordered solid solutions with surprisingly simple crystal structures, in contrast to many ordered intermetallic compounds [1,2]. Unique properties such as superior high-temperature strength, wear and oxidation resistance, and fatigue resistance [3–6], are attributed to the lack of a dominant solvent element, with the effects including severe lattice distortion and sluggish diffusion [7]. The impressive properties make MPEAs promising candidates for high-performance structural materials.

It is well-established that grain boundaries, as a planar defect, inhibit dislocation movement and increase materials' strength. However, they also act as preferred diffusion pathways and often nucleation sites for cracks. The grain size is sensitively dependent on processing conditions, including the cooling rate. Arc-melting and casting are frequently used fabrication methods for MPEAs, followed by a variety of homogenization treatments [8–11]. Fully characterizing the relationship between structure and processing via such serial casting and heat treatments requires the investment of significant time and resources. As a result, only a few cooling rate-controlled microstructural studies have been performed on MPEAs via Bridgman solidification [12–14]. An efficient method for producing and characterizing a wide range of microstructures could dramatically accelerate the design of these compositionally complex materials.

In this study, continuously graded compositional libraries of $Al_xCoCrFeNi$ are fabricated with the Laser Engineered Net Shaping (LENS™) process. Microstructural variations within a single library are achieved by controlling the laser power and travel speed during processing. The crystalline structure, microstructure and mechanical properties are characterized as a function of composition and processing condition and are compared with cast materials [15]. Using this high-throughput methodology, the processing-microstructure-property relationship in this MPEA is established.

2. Materials and methods

Raw materials including cobalt, chromium, iron and nickel (purity $\geq$ 99.95 wt %) were arc-melted in a water-cooled copper hearth using a tungsten electrode under an argon atmosphere, to produce ten equimolar alloy buttons. Each button was flipped and remelted at least 5 times to improve compositional homogeneity. The buttons were then melted together and cast into a copper mold

* Corresponding author. Department of Mechanical Engineering and Materials Science, Washington University in St. Louis, St. Louis, MO, 63130, USA.
E-mail address: floresk@wustl.edu (K.M. Flores).

https://doi.org/10.1016/j.jallcom.2020.154025
0925-8388/© 2020 Elsevier B.V. All rights reserved.

to produce a 20 mm × 12 mm × 4 mm plate. The plate was ground with 400 grit SiC paper and cleaned with methanol.

Three compositionally graded alloy libraries were prepared using an Optomec MR-7 LENS™ system. For each library, a 200 W laser traveling at 12.7 mm/s was used to create a melt pool on the surface of the CoCrFeNi substrate. Gas-atomized aluminum powder (Alfa-Aesar) with a reported purity of 99.5% (metals basis) was sieved to −100 + 325 mesh, resulting in a powder size range of 44–149 μm. The powder was deposited into the melt pool in 21 overlapping parallel lines spaced 0.5 mm apart, to form a single-layer, 19.05 mm × 10.16 mm patch, as shown in Fig. 1(a and b). Each track overlapped the previous track by approximately 25%. A continuous Al-content gradation was achieved by incrementally increasing the powder feed rate from 2.5 to 4.5 rpm over the span of the 21 parallel lines.

To produce microstructural variations, a total of 11 remelt lines, oriented parallel to the composition gradient and spaced at least 4 mm apart, were then remelted using different combinations of laser powers and travel speeds to achieve a desired range of quench rates, as illustrated in Fig. 1(c and d). These 11 lines were distributed over the 3 libraries, with 4 lines on two libraries, 3 lines on the third. The laser parameters for each line are shown in Table 1. The ratio of the laser travel speed to laser power, V_L/P_L, has been shown to correlate with the quench rate in laser processing [16]; $\dot{T}$ was calculated via a 3D finite element analysis (ABAQUS) [17] for each set of processing parameters, using experimentally derived thermal properties obtained from the literature [18]. These calculated quench rates are included in Table 1.

To expedite characterization of the alloy library, all of the microstructural measurements were performed in the plan view, i.e. perpendicular to the substrate surface, rather than in cross section. This saved time, since the samples did not need to be sectioned, and permitted the full range of compositional and microstructural variations within a given library to be viewed in a single microscopy session, on the same prepared surface. The top surfaces of the libraries were cleaned, ground with up to 1200 grit SiC paper and finally polished with 0.02 μm colloidal SiO_2 solution.

Due to the strong dependence of the local cooling rate on the position relative to the free surface [19], the amount of material removed by grinding and polishing was strictly controlled to be 0.25 mm for all the remelt samples. When necessary to improve contrast during imaging, samples were etched using an ethanol solution with 1.5 vol % HNO_3, 2.5 vol % H_2SO_4, and 6 vol % HCl.

The laser processed alloy microstructures were compared with a limited number of cast rods. Alloys with compositions of interest were pour-cast into copper molds to produce 3 mm and 4 mm diameter rods. The rods were cut in transverse sections from the middle of their length. The cooling rates for the cast cylindrical rods were estimated to be similar to iron rods with the same dimensions [20].

The microstructural variations along the centerline of each remelt line were characterized using a field emission scanning electron microscope (SEM, JEOL JSM-7001FLV). Care was taken to focus on the centerline and avoid imaging the heat affected zone along the edges of each remelted track. The local composition at each position of interest within the library was obtained using energy dispersive X-ray spectroscopy (EDS, Oxford Aztec Live X-Max Energy) on the SEM. Electron backscatter diffraction (EBSD, Oxford Symmetry) was used to determine the crystal structures of the observed phases.

To characterize the mechanical properties of the libraries, the microhardness of the alloys were measured as a function of composition and cooling rate using a 136° Vickers diamond pyramid (Leitz Miniload). The 200 g load was applied for 17 s. At least 6 indents were made for each composition and processing condition.

3. Results

The powder feed rates employed in the present work resulted in $Al_xCoCrFeNi$ alloys with Al contents of 11.28–23.78 at. % (x = 0.51–1.25), as is shown in Fig. 2. Although the thermal properties vary slightly with composition, for a given set of processing parameters, the finite element analysis of the laser heating process estimated similar quench rates for the compositions selected for

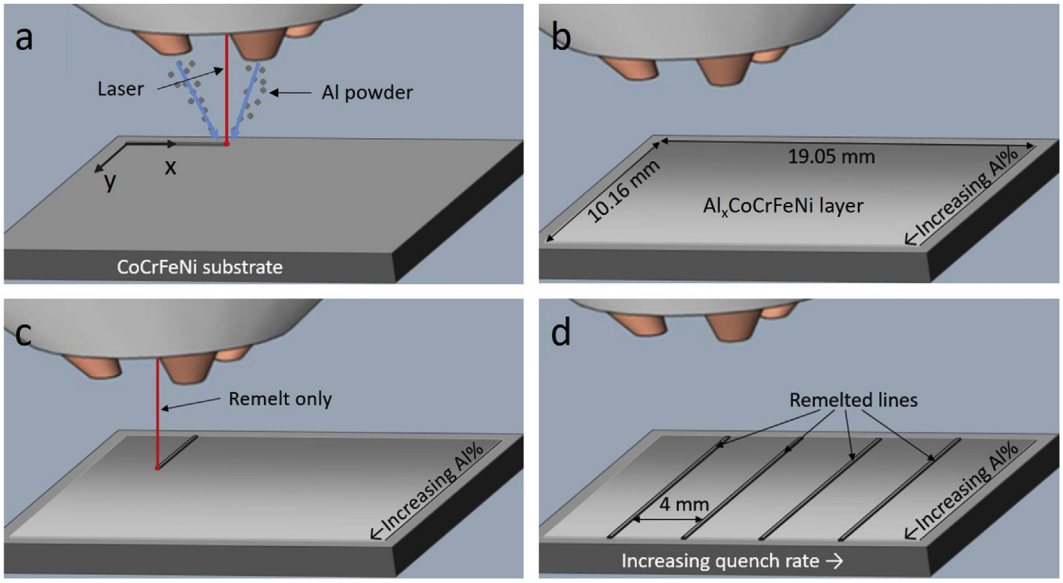

Fig. 1. In this schematic of the microstructural library fabrication process, (a) aluminum powder is deposited as the laser and powder nozzles traverse in 21 parallel, overlapping lines oriented in the x direction. (b) Increasing the powder feed rate in each sequential line produces a patch of alloyed material with the desired compositional gradient in the y direction. (c) The library is then remelted by the laser moving the in y direction, parallel to the Al concentration gradient. (d) Several well-spaced remelt lines are created using different combinations of laser power and travel speed to produce the desired range of quench rates.

Table 1
Laser parameters used to prepare the microstructural library, and the corresponding calculated cooling rates. To calculate the heat input, the laser spot size, $d = 1$ mm, is assumed to be constant with laser power.

Travel speed, V_L (mm/s)	Laser power, P_L (W)	Heat input, $L = \frac{P_L}{V_L d}$ (J/mm^2)	Cooling rate (K/s)		
			x = 0.56	x = 0.60	x = 1.00
38.1	100	2.62	6354	6402	5899
25.4	100	3.94	3472	3781	3805
38.1	150	3.94	4176	3488	4277
25.4	150	5.91	2479	2770	3393
12.7	150	11.8	1523	1589	1395
6.35	150	23.6	590	553	558
6.35	175	27.6	556	529	542
6.35	200	31.5	458	475	492
6.35	225	35.4	419	432	418
6.35	250	39.4	370	398	455
3.175	250	78.7	308	313	302
3 mm cast rod			48	48	48
4 mm cast rod			26	26	26

the microstructural study, as shown in Fig. 3.

Consistent with the microstructural observations in our prior work [15] and other work in the literature [21–24], at intermediate Al contents, $Al_xCoCrFeNi$ alloys have a duplex FCC + BCC microstructure. As can be seen in Fig. 4(a–c) (x = 0.56, $\dot{T}$ = 3472 K/s), cellular FCC crystals are embedded in a BCC matrix. A similar microstructure was obtained for all quench rates at this composition (Fig. 5(b–d)). This duplex structure is very sensitive to composition at higher quench rates, however. For a slightly higher Al fraction of x = 0.60, very little FCC phase was observed for quench rates exceeding 553 K/s, as shown in Fig. 4(d–f). The detailed FCC + BCC microstructural evolution with cooling rate for these compositions is shown in Fig. 5 and Supplementary Figs. S1(a–c). Based on SEM image contrast and EBSD, the BCC fraction was plotted against quench rate in Fig. 6.

At higher Al contents (e.g. Supplementary Figure S1(d-f), x = 1.00), the alloy also forms a cellular microstructure, however in this case both the interior and walls of the cells contain coherent BCC and B2 phases [15]. Consistent with prior work, the cell walls are enriched in Fe and Cr and have a woven BCC/B2 microstructure, while the interior of the cells consists of dispersed spherical BCC

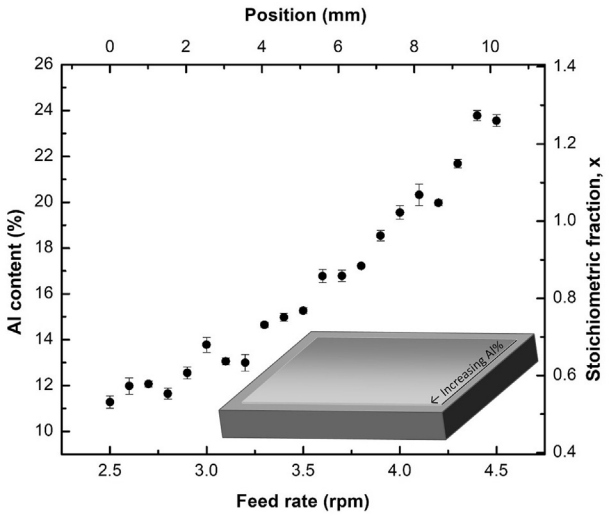

Fig. 2. The composition range of an $Al_xCoCrFeNi$ library determined by EDS, as a function of Al powder feed rate and position relative to the edge of the library. Each point corresponds to at least 4 measurements on each remelt line. Error bars indicate standard deviation.

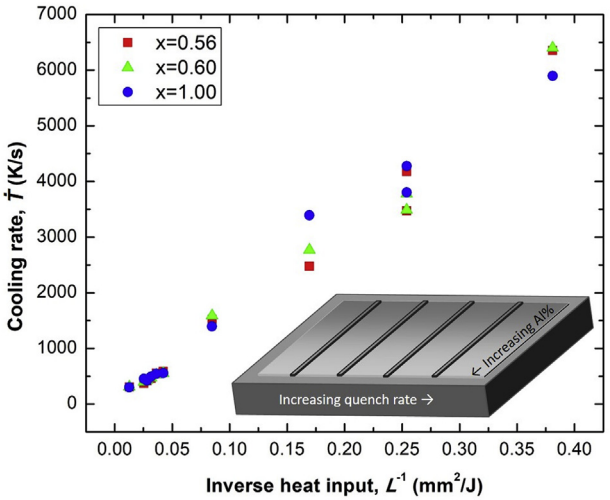

Fig. 3. Cooling rates for each alloy composition at 0.25 mm depth from the surface of the deposit, calculated using a finite element model, as a function of the inverse heat input.

nanoscale precipitates embedded in the B2 matrix (Supplementary Fig. S2) [15].

Vickers microhardness data obtained for each combination of composition and cooling rate is presented in Fig. 7(a). The BCC/B2 structure is generally observed to have a higher microhardness than the FCC + BCC structure. The hardness of both microstructures increases with cooling rate.

4. Discussion

4.1. Formation of the FCC + BCC microstructure at low Al content

Cellular and dendritic solidification are associated with constitutional undercooling of the liquid, which promotes the rapid, directional growth of small perturbations at the solid-liquid interface. In general during laser processing, different dendritic morphologies, from equiaxed, to tree-like structures with secondary branches, to cellular, can be obtained depending on the combination of the temperature gradient, G, and the velocity of the solid-liquid interface, R [25,26]. It has been shown experimentally that R is on the order of the laser travel speed [27]. The magnitude of the temperature gradient is a function of the laser heat input, which in turn depends on both the laser power and travel speed. The gradient can be resolved into two vector components, one parallel to laser travel direction, and the other normal to the substrate. The cellular microstructure obtained in this study can be attributed to a high G, resulting in highly directional growth, and moderate R, such that the transient secondary dendritic arms are given sufficient time to fully ripen and form columnar cells. Because the region of observation is well below the surface, at approximately at the mid-thickness of the melt pool, the columnar cells are primarily aligned perpendicular to the substrate, as reported in Ref. [26]. In this case, the cell growth direction is determined by both preferential crystallographic orientation as well as the direction of heat flow, which is anti-parallel to G.

Finer cellular microstructures were observed with increasing quench rate. As shown in Fig. 5(a), the size of the cellular structures, λ, observed in the FCC + BCC microstructures varies inversely with quench rate according to a power law, $\lambda = A \cdot \dot{T}^{-n}$ [28]. The fitting parameters, A and n, are presented in Table 2 [16,29–32], where they are compared with the values obtain from the literature for a

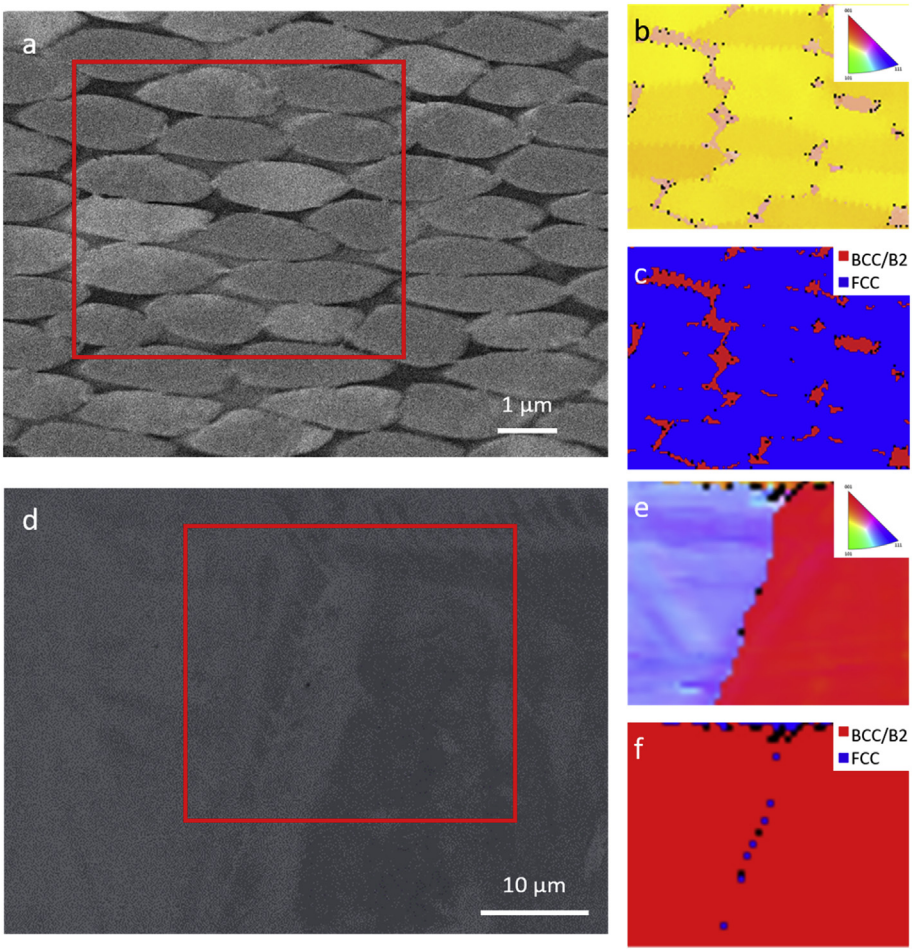

Fig. 4. Backscattered electron micrographs and their corresponding inverse pole figures and phase maps of (a–c) $Al_{0.56}CoCrFeNi$ processed at a cooling rate of 3472 K/s and (d–f) $Al_{0.60}CoCrFeNi$ processed at a cooling rate of 3781 K/s. Note that the slight increase in Al content destabilizes the formation of the FCC phase at this cooling rate.

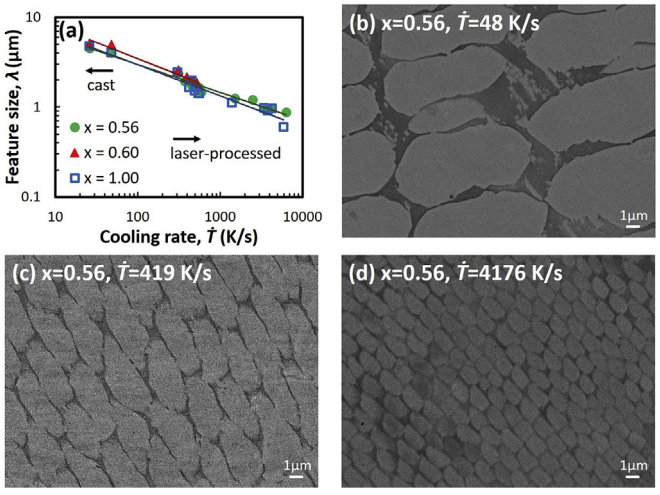

Fig. 5. The microstructural evolution with cooling rate for $Al_xCoCrFeNi$. (a) A decreasing trend in feature size with cooling rate for all the compositions is seen. The data for each composition were fitted to a power law relationship; fitting parameters are provided in Table 2. Backscattered electron images of x = 0.56 were obtained on (b) a 3 mm cast rod, and (c–d) the laser-processed library. The corresponding cooling rates are also indicated. Note that at higher cooling rates, a transition from FCC + BCC to BCC/B2 structure is observed at this composition. Similar micrographs for x = 0.60 and x = 1.00 are provided in Supplementary Fig. S1.

number of other alloys. Notably, the exponent n is approximately 1/3 for all of the alloys surveyed, including non-MPEAs. That is, all of the materials show a similar sensitivity to cooling rate, regardless of the compositional complexity of the alloy. Noting that the quench rate within the melt zone, $\dot{T}$, can be expressed as the product of G and R [26,33,34], models have been proposed that relate the

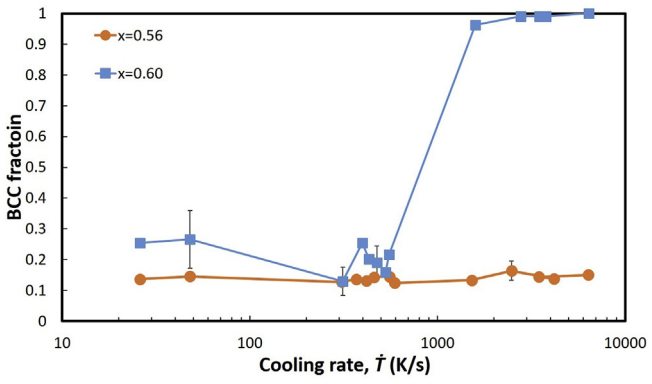

Fig. 6. The change in BCC fraction with cooling rate, as measured by the area fraction observed in SEM and EBSD. For x = 0.56, BCC fractions are relatively constant; for x = 0.60, the structure transitions to fully BCC at higher cooling rates.

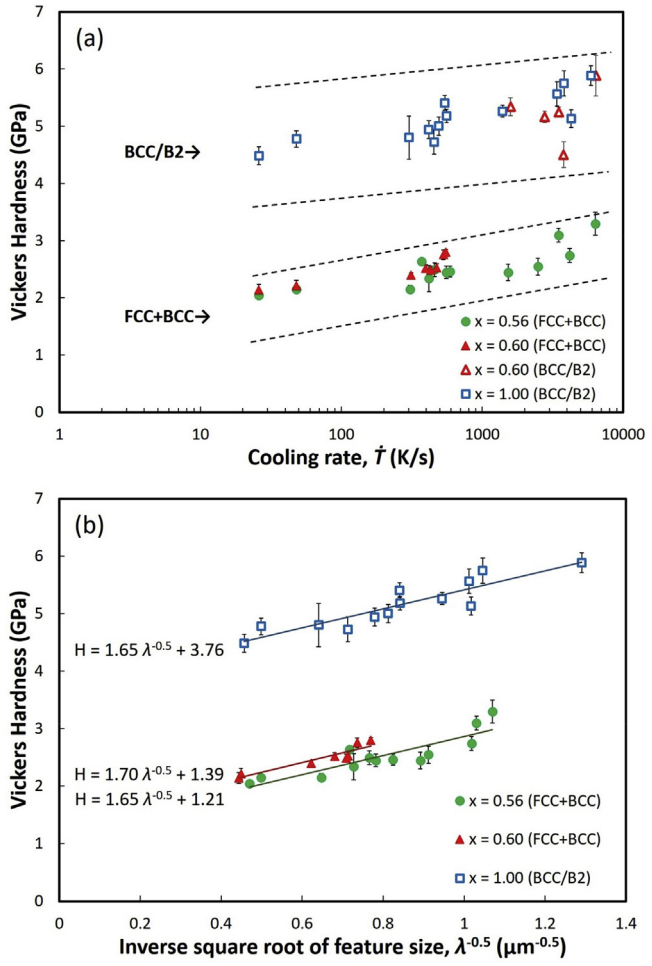

Fig. 7. Vickers microhardness as a function of (a) cooling rate and (b) inverse square root of microstructural feature size. Each data point corresponds to the average of at least 6 indents, and error bars indicate the standard deviation. With increasing cooling rate, the hardness increases for both structures. Notably, for x = 0.60 there is sudden increase in hardness values due to a change in the dominant phase. The microhardness is fitted to a Hall-Petch relationship in (b).

characteristic microstructural feature size to these parameters. Hunt [35] and Kurz and Fisher [36] considered the effect of the dendrite tip shape on the stability and spacing of the dendrite growth. Both models suggest that, in the velocity range of interest in this study, $\lambda \propto G^{-1/2}R^{-1/4}$. Several studies have reported that systems that adopt cellular structure with this dependency can also be satisfactorily fitted with a $\lambda \propto (GR)^{-1/3}$ power law, for instance aluminum [29,37] and magnesium alloys [32]. Indeed, Kirkaldy and Venugopalan [38] considered surface tension in addition to compositional segregation, and derived a formula with the form $\lambda \propto G^{-1/3}R^{-1/3}$. While the power law exponent in the present study is very similar to other systems and in general agreement with these models, the prefactor of the power law relationship, *A*, is much smaller for the MPEA compositions studied here, even in comparison to other laser processed materials. This suggests slower growth kinetics, probably due to the compositional complexity of the near-equiatomic liquid.

For x = 0.56, the BCC and FCC fractions are insensitive to cooling rate; only the size of the FCC features changes. In contrast, for x = 0.60, high quench rates suppress the formation of the cellular FCC features, most likely due to the slow diffusion of Al. Fig. 6 shows the BCC area fraction in $Al_{0.56}CoCrFeNi$ and $Al_{0.60}CoCrFeNi$ as a function of quench rate. For x = 0.60, the BCC fraction remains relatively constant at low quench rates, before a sudden jump to nearly 100% BCC for cooling rates of greater than 553 K/s. The resulting structure is similar to the BCC/B2 structure observed at higher Al contents. The sensitivity of the formation of the FCC phase to the Al content at high quench rate is most likely due to the severe lattice distortions associated with the addition of Al, which has a large atomic radius relative to the other constituents, to the FCC structure. This tends to stabilize the BCC/B2 structure, which has lower packing efficiency, and prevent significant growth of the FCC phase at high quench rates. Notably, the x = 0.60 BCC/B2 microstructure solidifies into a fully woven spinodal microstructure (similar to Supplementary Fig. S2(b)), in contrast to the combination of woven and nanoparticle structures described below for higher Al content. The lattice strain at x = 0.60 is apparently high enough to destabilize the FCC structure, but insufficient to promote significant coarsening of disordered BCC nanoparticles.

Table 2
Fitting parameters describing the relationship between feature size and cooling rate, $\lambda = A\dot{T}^{-n}$ [28]. Results from the present work are compared with other materials and processing techniques from the literature.

Source	*A*/μm	n	Material	Condition	DAS type
Gündüz [29]	28.8	0.32	Al-0.1 wt% Ti	DS	CS
	33.9	0.29	Al-0.5 wt% Ti		
Kaya [30]	39.6	0.28	Al-2 wt.% Li	DS	CS
Katayama [31]	25	0.28	310SS (Steel)	Laser	PDAS, CS
	80	0.33			SDAS
Bertoli [16]	N/A	0.33	316L (Steel)	Laser	CS
Luo [32]	44.75	0.28	Mg-0.60 wt% Gd	DS	CS
	54.96	0.27	Mg-1.38 wt% Gd		
	62.83	0.31	Mg-2.35 wt% Gd		
This work	12.44	0.31	$Al_{0.56}CoCrFeNi$	Laser	CS
	18.25	0.36	$Al_{0.60}CoCrFeNi$		
	14.66	0.35	AlCoCrFeNi		

PDAS/SDAS: primary/secondary dendrite arm spacing (dendrites with side branches), CS: cellular spacing, DS: directional solidification.

4.2. Formation of the BCC/B2 microstructure at high Al content

In contrast to the FCC + BCC microstructure at lower Al contents, at x = 1.00, both the cells and interdendritic regions exhibit BCC/B2 structures. Although the image contrast between the cells and matrix in Supplementary Figs. S1(d–f) results primarily from a microstructural transition, from BCC nanoparticles embedded in the B2 matrix within the cells to a woven spinodal sub-structure in the matrix, this cellular growth is still driven by constitutional undercooling; compositional variations between the cell interior and matrix have been reported elsewhere for both cast and laser-processed materials, where it was shown that Al and Ni segregate to the cell interior, while Fe and Cr are enriched in the cell walls [22,39]. It is therefore reasonable that the cell size, λ, follows a similar power law relationship as the FCC + BCC structure with *n* ~1/3. Surprisingly, both the low Al content (FCC + BCC structure) and high Al content (BCC/B2 structure) alloys have similar prefactors, *A*, for the power law relationship (Table 2), again reflecting the small cell size at a given quench rate. This insensitivity of the cell size to Al content, even for different crystal structures, suggests that the overall contributions of diffusivity, solute partitioning fraction, and freezing range to cell growth rate do not change significantly over the Al content range investigated.

4.3. Microstructural length scale effects on mechanical behavior

The Vickers microindention method used in this study produces indent sizes on the order of 25–40 μm, which is an order of

Table 3
Hall-Petch parameters for $Al_xCoCrFeNi$ multiprincipal element alloys, where H_0^c is overall intrinsic hardness, k^c is the overall Hall-Petch coefficient, and $k^{\alpha\beta}$ is the Hall-Petch coefficient for FCC-BCC phase boundaries. For reference, the microstructure-related parameters such as continuous phase fractions ($f_{\alpha c}$ and $f_{\beta c}$) and degree of separation (F_s), are also listed. For more information regarding how the topological parameters are measured and calculated, refer to Ref. [45]. For x = 0 (CoCrFeNi alloy), the overall intrinsic hardness (H_0^c) and overall Hall-Petch coefficient (k^c) are from Ref. [42].

	f_α	f_β	$f_{\alpha c}$	$f_{\beta c}$	F_s	H_0^c(GPa)	k^c(GPa μm$^{1/2}$)	$k^{\alpha\beta}$(GPa μm$^{1/2}$)
x = 0	1	0	1	0	0	1.16	1.62	–
x = 0.56	0.86	0.14	0.21	0.07	0.72	1.21	1.65	1.66
x = 0.60	0.80	0.20	0.03	0.06	0.90	1.39	1.70	1.71
x = 1	0	1	0	1	0	3.77	1.65	–

magnitude larger than the microstructural features for all quench rates considered in this work. Thus, the microhardness measurements are capable of capturing the influence of length scale refinement within the microstructural library. There is an overall increasing trend for hardness with quench rate for all of the compositions investigated. Notably, as shown in Fig. 7(a), the x = 0.60 BCC/B2 structure obtained at higher cooling rates exhibits hardness values comparable to the equimolar composition cooled at similar rates, which agrees with our previous study showing that the nanoindentation hardness of the BCC/B2 structure is relatively insensitive to the Al content [15].

As shown in Fig. 7(b), the microhardness follows a Hall-Petch relationship with cell size, $H = k \cdot \lambda^{-0.5} + H_0$. Here, k is the Hall-Petch coefficient, which describes the material's sensitivity to grain boundary strengthening, and H_0 is the material's intrinsic hardness. These fitting parameters are provided in Table 3 for the three compositions considered in this work. Compared to the FCC + BCC cellular structure, BCC/B2 has higher intrinsic hardness because of the reduced available dislocation slip systems relative to FCC, as we observed in our previous nanoindentation study of this alloy [15]. The intrinsic hardness of the FCC + BCC dual phase structures increases slightly from x = 0.56 to x = 0.60, which can be attributed to the higher fraction of the BCC/B2 phase.

The Hall-Petch relationship has only been established for a limited number of MPEAs. These studies have mainly considered single-phase FCC alloys, with the grain size controlled by different Bridgman solidification conditions [14] or by different annealing time and temperature [11,40–42]. Laser processing provides a way to quickly synthesize MPEA microstructural libraries and analyze the structure-property relationship. Although the intrinsic rapid solidification may give rise to thermal stresses, a relatively uniform shift is expected which should not affect the overall trend in the behavior.

For the three compositions of interest in this study, the values of the Hall-Petch coefficient, k, are quite similar, ranging 1.65–1.70. Wu et al. [43]. compared Hall-Petch coefficients of several different nanocrystalline metals and found that BCC-structured metals generally have larger k than FCC and HCP, due to a higher resolved shear stress required in BCC to operate a dislocation source near the grain boundary if using the dislocation pile-up model [44]. However, for two-phase materials, additional complexity can be anticipated. There are not only frictional stresses on the boundaries between grains of the same phase, but also interphase boundary contributions to hardness. Following Fan et al.'s extension of Hall-Petch relationship to two-ductile-phase alloys [45,46], the non-intrinsic hardness of the dual phase alloy (referred to as the α and β phases) is the summation of contributions from α-α and β-β grain boundaries as well as α-β interphase boundaries. The strengthening effects from all kinds of boundaries are linearly additive; however, in terms of influence on the Hall-Petch coefficient, the friction on the α-β phase boundaries could have a larger contribution. This is the case for the microstructural library in the current study, as shown in Table 3, where H_0^c is the overall intrinsic hardness, and k^c represents the overall Hall-Petch coefficient, corresponding to the fitting parameters in Fig. 7(b). At x = 0 (from Ref. [42]) and x = 1 (this work), k^c results solely from FCC and BCC/B2 grain boundaries, respectively, i.e. $k^c|_{x=0} = k^\alpha$ and $k^c|_{x=1} = k^\beta$. The Hall-Petch coefficient for the phase boundaries may be calculated using the following equation:

$$k^{\alpha\beta} = \frac{k^c - k^\alpha f_{\alpha c} - k^\beta f_{\beta c}}{F_s}$$

where $f_{\alpha c}$ and $f_{\beta c}$ (the continuous phase fractions) and F_s (degree of separation) are topological parameters which are calculated based on the phase fractions (f_α and f_β) and amount of phase boundaries (Table 3) [45,46]. The average values across all cooling rates for the three compositions considered are used in this calculation. The parameter $k^{\alpha\beta}$ is indicative of the effectiveness of strengthening of FCC-BCC phase boundaries; it is independent of phase fraction and composition, as can be seen in Table 3. All of the phase-fraction-related parameters in Table 3 are also listed; readers are referred to Fan et al.'s original work for additional details of the analysis [45,46].

To validate the parameters calculated in Table 3, the Vickers hardness as a function of feature size was calculated using Fan et al.'s model and compared with experimental values obtained from the laser-processed libraries at x = 0.51. The hardness was calculated from the Hall-Petch relationship,

$$H^c = H_0^c + k^c \cdot \lambda^{-0.5}$$

where H_0^c and k^c were evaluated using Fan's parameters:

$$H_0^c = H_0^\alpha f_{\alpha c} + H_0^\beta f_{\beta c} + H_0^{\alpha\beta} F_s$$

$$k^c = k^\alpha f_{\alpha c} + k^\beta f_{\beta c} + k^{\alpha\beta} F_s$$

Again, $f_{\alpha c}$, $f_{\beta c}$ and F_s can be obtained from the microstructures, and the phase-related Hall-Petch coefficients and intrinsic hardness are assumed to be insensitive to composition (here we used the average of values for x = 0.56 and 0.60). As shown in Fig. 8,

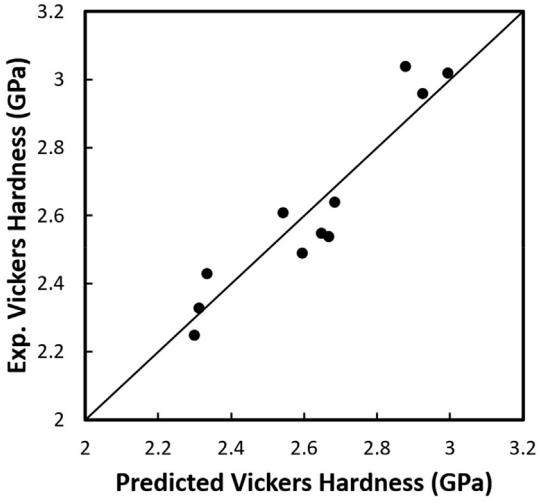

Fig. 8. Comparison between the Vickers hardness of $Al_{0.51}CoCrFeNi$ calculated using Fan et al.'s model [45] and the experimentally obtained results.

there is excellent agreement between the calculated and experimental results.

5. Conclusions

Compositional and microstructural libraries of $Al_xCoCrFeNi$ were successfully fabricated using a high-throughput laser deposition technique. The quench rate was varied over a range of 26–6400 K/s by adjusting the laser power and travel speed during remelting of the compositional library. The resulting cellular microstructures were very similar to those observed in cast materials, with the dual FCC + BCC structure observed at low Al contents transitioning to a BCC/B2 structure at near the equimolar composition. Microstructural and microhardness variations with quench rate were characterized using the libraries. The observed cellular microstructure becomes finer with increasing cooling rate, following a power law of the form $\lambda = A \cdot \dot{T}^{-1/3}$, similar to many other alloys. Microstructural refinement results in increasing microhardness, following a Hall-Petch relationship. The relative contributions of grain and interphase boundaries to the hardness of the dual phase FCC + BCC structures were also resolved in this study. The significant reduction in the time required to produce a wide array of compositions and microstructures gives laser processing the potential to accelerate the study of processing-microstructure-mechanical property relationships for complex, multicomponent alloys.

Declaration of competing interest

The authors declare that they have no known competing financial interests or personal relationships that could have appeared to influence the work reported in this paper.

CRediT authorship contribution statement

Mu Li: Conceptualization, Methodology, Formal analysis, Writing - original draft. **Katharine M. Flores:** Conceptualization, Writing - review & editing.

Acknowledgements

This work was supported by the National Science Foundation, Grant No. DMR-1809571. The authors also acknowledge financial support from Washington University in St. Louis and the Institute of Materials Science and Engineering for the use of shared instruments and staff assistance.

Appendix A. Supplementary data

Supplementary data to this article can be found online at https://doi.org/10.1016/j.jallcom.2020.154025.

References

[1] B. Cantor, Multicomponent and high entropy alloys, Entropy 16 (2014) 4749–4768, https://doi.org/10.3390/e16094749.
[2] J.W. Yeh, Recent progress in high-entropy alloys, Ann. Chimie Sci. Matériaux 31 (2006) 633–648, https://doi.org/10.3166/acsm.31.633-648.
[3] C.-J. Tong, Y.-L. Chen, J.-W. Yeh, S.-J. Lin, S.-K. Chen, T.-T. Shun, C.-H. Tsau, S.-Y. Chang, Mechanical performance of the AlxCoCrCuFeNi high-entropy alloy system with multiprincipal elements, Metall. Mater. Trans. A 36 (2005) 881–893, https://doi.org/10.1007/s11661-005-0283-0.
[4] J.M. Wu, S.J. Lin, J.W. Yeh, S.K. Chen, Y.S. Huang, H.C. Chen, Adhesive wear behavior of AlxCoCrCuFeNi high-entropy alloys as a function of aluminum content, Wear 261 (2006) 513–519, https://doi.org/10.1016/j.wear.2005.12.008.
[5] P. Huang, J. Yeh, Multi-principal element alloys with improved oxidation and wear resistance for thermal spray coating, Adv. Eng. Mater. 6 (2004) 74–78, https://doi.org/10.1002/adem.200300507.
[6] M.A. Hemphill, T. Yuan, G.Y. Wang, J.W. Yeh, C.W. Tsai, A. Chuang, P.K. Liaw, Fatigue behavior of Al0.5CoCrCuFeNi high entropy alloys, Acta Mater. 60 (2012) 5723–5734, https://doi.org/10.1016/j.actamat.2012.06.046.
[7] Y. Zhang, T.T. Zuo, Z. Tang, M.C. Gao, K.A. Dahmen, P.K. Liaw, Z.P. Lu, Microstructures and properties of high-entropy alloys, Prog. Mater. Sci. 61 (2014) 1–93, https://doi.org/10.1016/j.pmatsci.2013.10.001.
[8] Y.-F. Kao, T.-J. Chen, S.-K. Chen, J.-W. Yeh, Microstructure and mechanical property of as-cast, -homogenized, and -deformed AlxCoCrFeNi ($0 \le x \le 2$) high-entropy alloys, J. Alloys Compd. 488 (2009) 57–64, https://doi.org/10.1016/j.jallcom.2009.08.090.
[9] S.T. Chen, W.Y. Tang, Y.F. Kuo, S.Y. Chen, C.H. Tsau, T.T. Shun, J.W. Yeh, Microstructure and properties of age-hardenable AlxCrFe1.5MnNi0.5 alloys, Mater. Sci. Eng. A 527 (2010) 5818–5825, https://doi.org/10.1016/j.msea.2010.05.052.
[10] N.N. Guo, L. Wang, L.S. Luo, X.Z. Li, Y.Q. Su, J.J. Guo, H.Z. Fu, Microstructure and mechanical properties of refractory MoNbHfZrTi high-entropy alloy, Mater. Des. 81 (2015) 87–94, https://doi.org/10.1016/j.matdes.2015.05.019.
[11] F. Otto, A. Dlouhý, C. Somsen, H. Bei, G. Eggeler, E.P. George, The influences of temperature and microstructure on the tensile properties of a CoCrFeMnNi high-entropy alloy, Acta Mater. 61 (2013) 5743–5755, https://doi.org/10.1016/j.actamat.2013.06.018.
[12] S.G. Ma, S.F. Zhang, M.C. Gao, P.K. Liaw, Y. Zhang, A successful synthesis of the CoCrFeNiAl0.3 single-crystal, high-entropy alloy by Bridgman solidification, JOM (J. Occup. Med.) 65 (2013) 1751–1758, https://doi.org/10.1007/s11837-013-0733-x.
[13] Y. Zhang, S.G. Ma, J.W. Qiao, Morphology transition from dendrites to equiaxed grains for AlCoCrFeNi high-entropy alloys by copper mold casting and Bridgman solidification, Metall. Mater. Trans. A 43 (2012) 2625–2630, https://doi.org/10.1007/s11661-011-0981-8.
[14] S.G. Ma, S.F. Zhang, J.W. Qiao, Z.H. Wang, M.C. Gao, Z.M. Jiao, H.J. Yang, Y. Zhang, Superior high tensile elongation of a single-crystal CoCrFeNiAl 0.3 high-entropy alloy by Bridgman solidification, Intermetallics 54 (2014) 104–109, https://doi.org/10.1016/j.intermet.2014.05.018.
[15] M. Li, J. Gazquez, A. Borisevich, R. Mishra, K.M. Flores, Evaluation of microstructure and mechanical property variations in AlxCoCrFeNi high entropy alloys produced by a high-throughput laser deposition method, Intermetallics 95 (2018) 110–118, https://doi.org/10.1016/j.intermet.2018.01.021.
[16] U. Scipioni Bertoli, G. Guss, S. Wu, M.J. Matthews, J.M. Schoenung, In-situ characterization of laser-powder interaction and cooling rates through high-speed imaging of powder bed fusion additive manufacturing, Mater. Des. 135 (2017) 385–396, https://doi.org/10.1016/j.matdes.2017.09.044.
[17] H. Sun, Microstructure Evolution of Bulk Metallic Glasses via Laser Processing, The Ohio State University, 2010.
[18] S. Uporov, V. Bykov, S. Pryanichnikov, A. Shubin, N. Uporova, Effect of synthesis route on structure and properties of AlCoCrFeNi high-entropy alloy, Intermetallics 83 (2017) 1–8, https://doi.org/10.1016/j.intermet.2016.12.003.
[19] H. Sun, K.M. Flores, Microstructural analysis of a laser-processed Zr-based bulk metallic glass, Metall. Mater. Trans. A 41 (2010) 1752–1757, https://doi.org/10.1007/s11661-009-0151-4.
[20] M. Górny, E. Tyrała, Effect of cooling rate on microstructure and mechanical properties of thin-walled ductile iron castings, J. Mater. Eng. Perform. 22 (2013) 300–305, https://doi.org/10.1007/s11665-012-0233-0.
[21] T. Yang, S. Xia, S. Liu, C. Wang, S. Liu, Y. Zhang, J. Xue, S. Yan, Y. Wang, Effects of AL addition on microstructure and mechanical properties of AlxCoCrFeNi High-entropy alloy, Mater. Sci. Eng. A 648 (2015) 15–22, https://doi.org/10.1016/j.msea.2015.09.034.
[22] Y. Ma, B. Jiang, C. Li, Q. Wang, C. Dong, P. Liaw, F. Xu, L. Sun, The BCC/B2 morphologies in AlxNiCoFeCr high-entropy alloys, Metals 7 (2017) 57, https://doi.org/10.3390/met7020057.
[23] J. Joseph, T. Jarvis, X. Wu, N. Stanford, P. Hodgson, D.M. Fabijanic, Comparative study of the microstructures and mechanical properties of direct laser fabricated and arc-melted Al x CoCrFeNi high entropy alloys, Mater. Sci. Eng. A 633 (2015) 184–193, https://doi.org/10.1016/j.msea.2015.02.072.
[24] W.-R. Wang, W.-L. Wang, S.-C. Wang, Y.-C. Tsai, C.-H. Lai, J.-W. Yeh, Effects of Al addition on the microstructure and mechanical property of AlxCoCrFeNi high-entropy alloys, Intermetallics 26 (2012) 44–51, https://doi.org/10.1016/j.intermet.2012.03.005.
[25] B. Zheng, Y. Zhou, J.E. Smugeresky, J.M. Schoenung, E.J. Lavernia, Thermal behavior and microstructure evolution during laser deposition with laser-engineered Net shaping: Part II. Experimental investigation and discussion, Metall. Mater. Trans. A 39 (2008) 2237–2245, https://doi.org/10.1007/s11661-008-9566-6.
[26] H. Yin, S.D. Felicelli, Dendrite growth simulation during solidification in the LENS process, Acta Mater. 58 (2010) 1455–1465, https://doi.org/10.1016/j.actamat.2009.10.053.
[27] M. Gäumann, S. Henry, F. Cléton, J.-D. Wagnièe, W. Kurz, Epitaxial Laser Metal Forming: Analysis of Microstructure Formation, 1999, https://doi.org/10.1016/S0921-5093(99)00202-6.
[28] M. Flemings, Solidification Processing, McGraw-Hill, New York, 1974.
[29] M. Gündüz, H. Kaya, E. Çadırlı, N. Maraşlı, K. Keşlioğlu, B. Saatçi, Effect of solidification processing parameters on the cellular spacings in the Al–0.1wt% Ti and Al–0.5wt% Ti alloys, J. Alloys Compd. 439 (2007) 114–127, https://doi.org/10.1016/j.jallcom.2006.08.246.
[30] H. Kaya, E. Çadırlı, M. Gündüz, Directional cellular growth of Al-2 wt% Li bulk

samples, Appl. Phys. A 94 (2009) 155–165, https://doi.org/10.1007/s00339-008-4714-9.
[31] S. Katayama, A. Matsunawa, Solidification microstructure of laser welded stainless steels, in: Int. Congr. Appl. Lasers Electro-Optics, Laser Institute of America, 1984, pp. 60–67, https://doi.org/10.2351/1.5057623.
[32] S. Luo, G. Yang, S. Liu, J. Wang, J. Li, W. Jie, Microstructure evolution and mechanical properties of directionally solidified Mg-xGd (x=0.8, 1.5, and 2.5) alloys, Mater. Sci. Eng. A 662 (2016) 241–250, https://doi.org/10.1016/j.msea.2016.03.065.
[33] M. Gäumann, C. Bezençon, P. Canalis, W. Kurz, Single-crystal laser deposition of superalloys: processing–microstructure maps, Acta Mater. 49 (2001) 1051–1062, https://doi.org/10.1016/S1359-6454(00)00367-0.
[34] S. Bontha, N.W. Klingbeil, P.A. Kobryn, H.L. Fraser, Thermal process maps for predicting solidification microstructure in laser fabrication of thin-wall structures, J. Mater. Process. Technol. 178 (2006) 135–142, https://doi.org/10.1016/j.jmatprotec.2006.03.155.
[35] J.D. Hunt, Solidification and Castings of Metals, The Metals Society, London, 1979.
[36] W. Kurz, D.J. Fisher, Dendrite growth at the limit of stability: tip radius and spacing, Acta Metall. 29 (1981) 11–20, https://doi.org/10.1016/0001-6160(81)90082-1.
[37] H. Kaya, M. Gündüz, E. Çadırlı, N. Maraşlı, Dependency of microindentation hardness on solidification processing parameters and cellular spacing in the directionally solidified Al based alloys, J. Alloys Compd. 478 (2009) 281–286, https://doi.org/10.1016/j.jallcom.2008.11.164.
[38] J. Kirkaldy, D. Venugopalan, Pattern selection relations for deep-rooted binary alloy cells, Scripta Metall. 23 (1989) 1603–1608, https://doi.org/10.1016/0036-9748(89)90137-3.
[39] V. Ocelík, N. Janssen, S.N. Smith, J.T.M. De Hosson, Additive manufacturing of high-entropy alloys by laser processing, J. Occup. Med. 68 (2016) 1810–1818, https://doi.org/10.1007/s11837-016-1888-z.
[40] B. Gwalani, V. Soni, M. Lee, S. Mantri, Y. Ren, R. Banerjee, Optimizing the coupled effects of Hall-Petch and precipitation strengthening in a Al 0.3 CoCrFeNi high entropy alloy, Mater. Des. 121 (2017) 254–260, https://doi.org/10.1016/j.matdes.2017.02.072.
[41] W.H. Liu, Y. Wu, J.Y. He, T.G. Nieh, Z.P. Lu, Grain growth and the Hall–Petch relationship in a high-entropy FeCrNiCoMn alloy, Scripta Mater. 68 (2013) 526–529, https://doi.org/10.1016/j.scriptamat.2012.12.002.
[42] Z. Wu, H. Bei, F. Otto, G.M. Pharr, E.P. George, Recovery, recrystallization, grain growth and phase stability of a family of FCC-structured multi-component equiatomic solid solution alloys, Intermetallics 46 (2014) 131–140, https://doi.org/10.1016/j.intermet.2013.10.024.
[43] D. Wu, J. Zhang, J.C. Huang, H. Bei, T.G. Nieh, Grain-boundary strengthening in nanocrystalline chromium and the Hall–Petch coefficient of body-centered cubic metals, Scripta Mater. 68 (2013) 118–121, https://doi.org/10.1016/j.scriptamat.2012.09.025.
[44] M. Srinivas, G. Malakondaiah, R.W. Armstrong, P. Rama Rao, Ductile fracture toughness of polycrystalline armco iron of varying grain size, Acta Metall. Mater. 39 (1991) 807–816, https://doi.org/10.1016/0956-7151(91)90280-E.
[45] Z. Fan, P. Tsakiropoulos, P.A. Smith, A.P. Miodownik, Extension of the Hall-Petch relation to two-ductile-phase alloys, Philos. Mag. A 67 (1993) 515–531, https://doi.org/10.1080/01418619308207175.
[46] Z. Fan, P. Tsakiropoulos, A.P. Miodownik, A generalized law of mixtures, J. Mater. Sci. 29 (1994) 141–150, https://doi.org/10.1007/BF00356585.